JCI insight

Purkinje cell–specific deficiency in SEL1L-HRD1 endoplasmic reticulum–associated degradation causes progressive cerebellar ataxia in mice

Mauricio Torres,[1] Brent Pederson,[2] Hui Wang,[1] Liangguang Leo Lin,[1] Huilun Helen Wang,[1] Amara Bugarin-Lapuz,[2] Zhen Zhao,[3] and Ling Qi[1,2]

[1]Department of Molecular Physiology and Biological Physics, University of Virginia, Charlottesville, Virginia, USA.

[2]Department of Molecular & Integrative Physiology, University of Michigan Medical School, Ann Arbor, Michigan, USA.

[3]Zilkha Neurogenetic Institute, Keck School of Medicine of USC, Los Angeles, California, USA.

Recent studies have identified multiple genetic variants of SEL1L-HRD1 endoplasmic reticulum–associated degradation (ERAD) in humans with neurodevelopmental disorders and locomotor dysfunctions, including ataxia. However, the relevance and importance of SEL1L-HRD1 ERAD in the pathogenesis of ataxia remain unexplored. Here, we showed that SEL1L deficiency in Purkinje cells leads to early-onset progressive cerebellar ataxia with progressive loss of Purkinje cells with age. Mice with Purkinje cell–specific deletion of SEL1L (*Sel1L*^{Pcp2Cre}) exhibited motor dysfunction beginning around 9 weeks of age. Transmission electron microscopy analysis revealed dilated ER and fragmented nuclei in Purkinje cells of adult *Sel1L*^{Pcp2Cre} mice, indicative of altered ER homeostasis and cell death. Finally, loss of Purkinje cells was associated with a secondary neurodegeneration of granular cells, as well as robust activation of astrocytes and proliferation of microglia, in the cerebellums of *Sel1L*^{Pcp2Cre} mice. These data demonstrate the pathophysiological importance of SEL1L-HRD1 ERAD in Purkinje cells in the pathogenesis of cerebellar ataxia.

Introduction

Endoplasmic reticulum–associated degradation (ERAD) is a conserved quality control pathway responsible for the removal of misfolded proteins in the endoplasmic reticulum (ER) for proteasomal degradation in the cytosol (1–3). The suppressor of lin-12-like–HMG-CoA reductase degradation 1 (SEL1L-HRD1) complex represents the most conserved branch of ERAD from yeast to humans (4–6), with SEL1L being the cognate cofactor for the E3 ligase HRD1 (4, 7, 8). Using germline- and inducible-KO mouse models, we and others have shown that SEL1L-HRD1 ERAD is indispensable for embryonic and adult development in vivo (7, 9–11). Recent studies using cell-type-specific KO mouse models have revealed the vital importance of SEL1L and HRD1 in a cell-type- and substrate-specific manner in various physiological processes, including food intake, water balance, immune function, stem cell biology, and energy homeostasis (2, 12–35). Importantly, we recently identified 4 pathogenic SEL1L-HRD1 ERAD variants in 11 patients from 4 families, which are characterized by infantile-onset developmental delay, intellectual disability, microcephaly, facial dysmorphisms, hypotonia, and/or ataxia (36–38). We termed this rare neurodevelopmental disorder as ERAD-associated neurodevelopmental disorders with onset in infancy (ENDI) (36). Moreover, the SEL1L S658P variant initially identified in Finnish Hounds with cerebellar ataxia (39) was recently reported to cause early-onset, nonprogressive ataxia in the mouse model expressing the variant (40). While the patients exhibit impaired balance and coordination, the direct role of neuronal SEL1L-HRD1 ERAD in human ataxia remains unknown.

Cerebellar ataxia is a neurological disorder characterized by degeneration of the cerebellum and its associated structures, affecting motor control, balance, and coordination, leading to difficulties in walking and problems with fine motor skills and speech (41). Purkinje cells are a type of neuron found in the cerebellum and are characterized by their elaborate dendritic arbors (42). Dysfunction or degeneration of Purkinje cells can lead to a variety of diseases, including cerebellar ataxia (43). Previous studies in both patients and mouse model systems have implicated several dozen cytosolic and nuclear proteins in

Conflict of interest: The authors have declared that no conflict of interest exists.

Submitted: August 10, 2023
Accepted: September 24, 2024
Published: October 1, 2024

Reference information: *JCI Insight*. 2024;9(21):e174725. https://doi.org/10.1172/jci.insight.174725.

the pathogenesis of ataxia, but very few ER proteins (41, 44). Mutations in inositol 1,4,5-trisphosphate receptor type 1 (ITPR1), an ER calcium channel, have been identified in early-onset, nonprogressive, mild spinocerebellar ataxia type 29 (SCA29, OMIM #117360) (45, 46). However, the importance of ER protein folding and degradation in the onset and progression of cerebellar ataxia remains unknown.

Here, we report an indispensable role of SEL1L and, by extension, SEL1L-HRD1 ERAD, in cerebellar ataxia. The Purkinje cell–specific *Sel1L*-deficient mouse model (*Sel1L*^{Pcp2Cre}) grew comparably to their WT littermates and appeared indistinguishable in gait and balance beam tests at 6 weeks of age; however, they exhibited deteriorating motor function with age, including asymmetric gait, loss of balance, and coordination deficits. Mechanistically, we further showed that SEL1L-HRD1 ERAD deficiency lead to a progressive Purkinje cell neurodegeneration with dilated ER and fragmented nuclei. These findings establish SEL1L-HRD1 ERAD as a key player in Purkinje cells in the pathogenesis of cerebellar ataxia.

Results

Generation of Sel1L^{Pcp2Cre} *mice with Purkinje cell–specific deletion of SEL1L*. To explore the role of SEL1L-HRD1 ERAD in cerebellar ataxia, we generated *Sel1L*^{Pcp2Cre} mice with Purkinje cell–specific deletion of Sel1L by crossing *Sel1L*$^{fl/fl}$ mice (7) with a transgenic mouse expressing Cre recombinase driven by the promoter of Purkinje cell protein 2 (*Pcp2)* (47). Pcp2 promoter becomes active starting within the first postnatal week (48). Both male and female *Sel1L*^{Pcp2Cre} mice grew comparably to *Sel1L*$^{fl/fl}$ WT littermates from 3 to 20 weeks of age (Figure 1, A–C). Brain weights were comparable between the cohorts at 12 weeks of age but were decreased by 10% in *Sel1L*^{Pcp2Cre} mice at 20 weeks of age compared with those of WT littermates (Figure 1, D–F). Protein levels of both SEL1L and HRD1 were reduced by 60% and 40%, respectively, in total cerebellar lysates from 5-week-old mice (Figure 1, G and H). This observation is in line with our previous reports showing the requirement of SEL1L in HRD1 stability (7). Deletion of SEL1L in Purkinje cells was further confirmed using confocal microscopy, which showed an 80% reduction of SEL1L signal in Purkinje cells (Figure 1, I and J). Protein level of ERAD cofactor OS9 (also an ERAD substrate) was doubled in the cerebellum of 5-week-old *Sel1L*^{Pcp2Cre} mice (Figure 1, G and H), pointing to SEL1L-HRD1 ERAD dysfunction. By contrast, SEL1L protein level in granule cells was not changed (Figure 1K).

Purkinje cell SEL1L deficiency leads to progressive cerebellar ataxia. At 6 weeks of age, *Sel1L*^{Pcp2Cre} mice displayed similar gait (Figure 2, A–C) and performance in balance beam tests (Figure 2, D and E, and Supplemental Video 1; supplemental material available online with this article; https://doi.org/10.1172/jci.insight.174725DS1) as their WT littermates. By 12 weeks, *Sel1L*^{Pcp2Cre} mice showed progressively worsening asymmetric gait, evidenced by increased distance between paw match placements and a wider gap between footprints (Figure 2C and Supplemental Video 2). Additionally, 12-week-old *Sel1L*^{Pcp2Cre} mice took significantly longer to cross the balance beam (Figure 2, D and E, and Supplemental Video 3) and frequently used their tails to prevent falling (Supplemental Video 3 and Figure 2D). Performance further declined in both tests at 18 and 22 weeks of age (Figure 2, C and E). Similarly, the hind limb–clasping reflex (49) was comparable between the 2 groups at 6 and 12 weeks but became abnormal at 18 and 22 weeks (Figure 2, F and G). Taken together, these data show that Purkinje cell–specific SEL1L-HRD1 ERAD deficiency leads to progressive cerebellar ataxia.

Progressive loss of Purkinje cells in Sel1L^{Pcp2Cre} *mice with age*. Purkinje cells typically exhibit a prominent soma located in a continuous line between the granular and molecular layers of the cerebellum (arrowheads, Figure 3A). Histological examination of the cerebellum revealed comparable Purkinje cell numbers between the cohorts at 5 weeks of age (Figure 3, A and D), but these numbers progressively reduced from 50% to 20% in *Sel1L*^{Pcp2Cre} mice at 12- and 20-week of age compared with their WT littermates (Figure 3, B–D). Confocal microscopic analyses of the Purkinje cell marker calbindin further demonstrated the progressive loss of Purkinje cells with age in *Sel1L*^{Pcp2Cre} mice (Figure 4, A–C), which was supported by Western blot analyses of calbindin protein levels in the cerebellar lysates (Figure 4, E and F). In both assays, Purkinje cell number progressively reduced from 40% to 50% at 12 weeks to 10% to 20% at 20 weeks in *Sel1L*^{Pcp2Cre} mice, compared with those of WT littermates (Figure 4, D and F). Concomitantly, we observed a nearly 40% reduction in the number of granule cells (Figure 3, C and E) and a 60% reduction in the molecular layer of *Sel1L*^{Pcp2Cre} mice at 20 weeks of age (Figure 3, F and G), in line with the known effects of Purkinje cell deficiency on granule cells and molecular layer (50–52).

ER expansion and Purkinje cell neurodegeneration in the absence of SEL1L. We next evaluated the ER ultrastructure of Purkinje cells in the cerebellum of 5- and 9-week-old mice using transmission electron

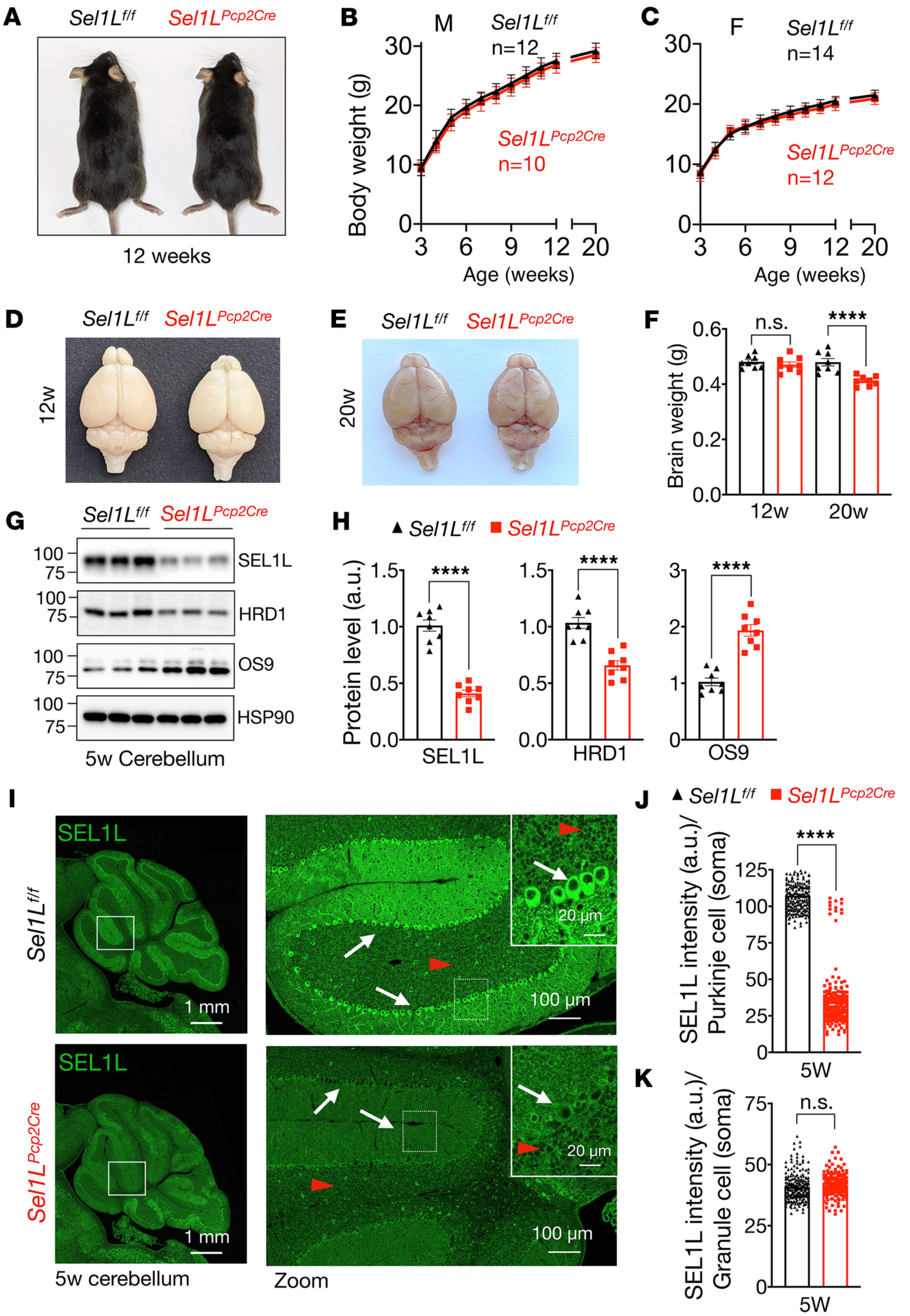

Figure 1. Generation of a mouse model with ERAD deficiency in Purkinje cells. (**A**) Representative images of 12-week-old *Sel1L*$^{f/f}$ (WT) and *Sel1L*^{Pcp2Cre} (Sel1L-KO) male mice. (**B** and **C**) Growth curve for male (**B**) and female (**C**) *Sel1L*$^{f/f}$ and *Sel1L*^{Pcp2Cre} mice (3–20 weeks, *n* = 10–14 mice per group). (**D** and **E**) Representative images of brains from 12- and 20-week-old mice. (**F**) Quantitation of brain weight from 12- and 20-week-old mice (*n* = 8 mice per group). (**G**) Western blot analysis of cerebellar protein extracts at 5 weeks of age with quantitation showed in **H** (*n* = 8 mice per group). Values shown are in kDa. (**I**) Immunofluorescence of Sel1L protein in cerebellum tissue at 5 weeks of age, showing high-magnification images (insets) for granule cells (red arrowheads) and Purkinje cells (white arrows), with quantitation of SEL1L signal intensity in the soma of Purkinje cells in **J** and granule cells in **K**. Measurements obtained from 180 to 200 cells (*n* = 3 mice per group). Data are shown as the mean ± SEM. ****$P < 0.0001$ by 2-way ANOVA followed by Bonferroni's multiple comparisons test (**B** and **C**) and *t* test (**F**, **H**, **J**, and **K**). Scale bar: 1 mm (**I**, first column); 100 μm (**I**, second column); 20 μm (**I**, inset).

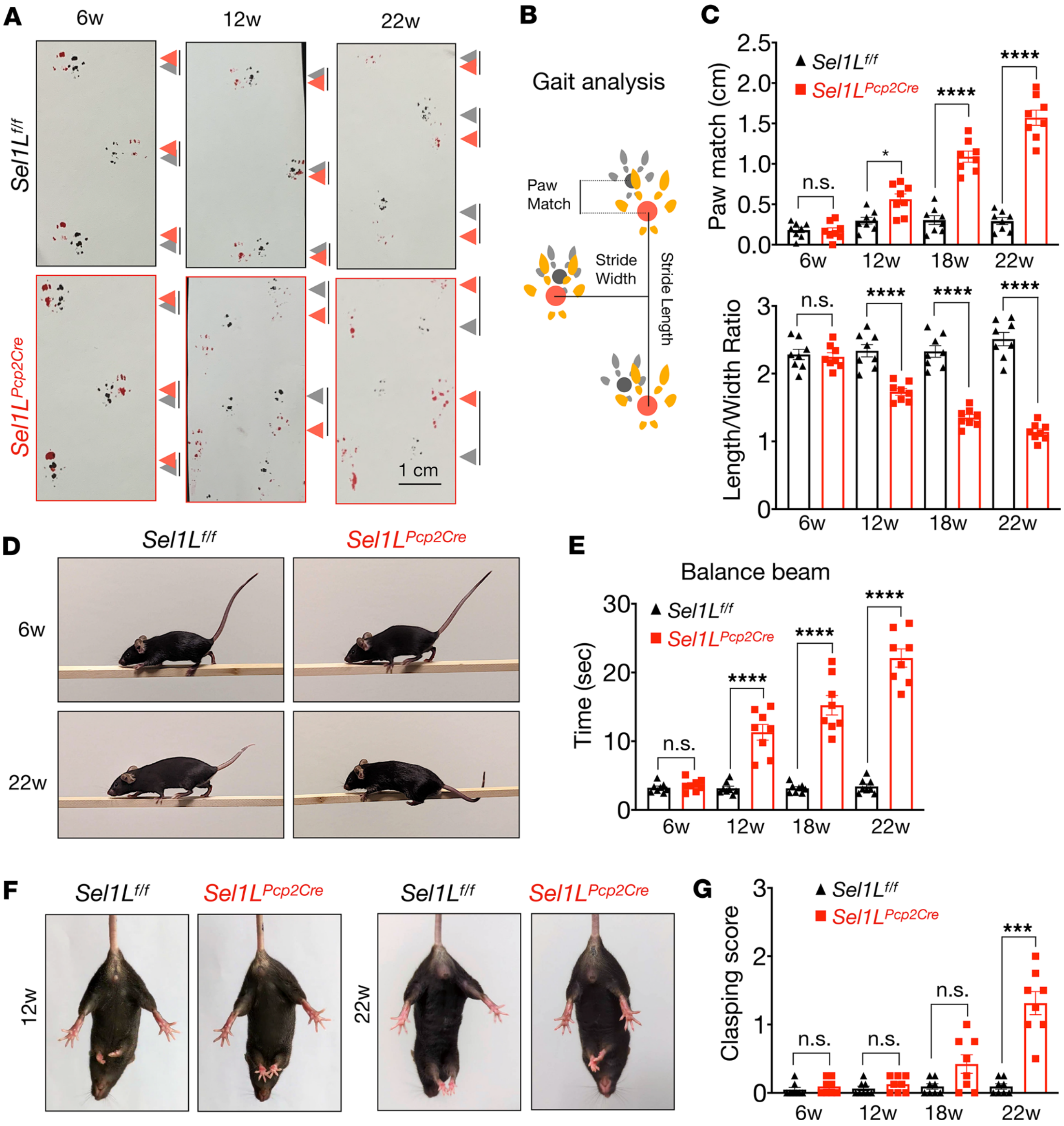

Figure 2. *Sel1L*^{Pcp2Cre}-KO mice exhibit progressive cerebellar ataxia. (**A**) Representative images of paw prints from 6-, 12-, and 22-week-old mice showing gait analysis for Sel1L$^{f/f}$ and Sel1L^{Pcp-2} mice. The gray and red arrows indicate forelimb and hindlimb, respectively. Lines between gray and red arrows indicate distance between 2 limbs. (**B**) Cartoon schematic of the gait analysis. (**C**) Quantitation of gait analysis of 6- to 22-week-old littermates of both sexes ($n = 8$ mice per group). (**D**) Representative images of balance beam test from 6- and 22-week-old mice. (**E**) Quantitation of balance beam test from mice at 6, 12, 18, and 22 weeks of ages ($n = 8$ mice per group). (**F**) Representative images of hindlimb clasping of 12- and 22-week-old mice. (**G**) Quantification of hindlimb clasping from mice at 6, 12,18, and 22 weeks of age ($n = 8$ mice per group). Data are shown as the mean ± SEM. ***$P < 0.001$, ****$P < 0.0001$ by 2-way ANOVA followed by Bonferroni's multiple comparisons test (**C**, **E**, and **G**). Scale bar: 1 cm (**A**).

microscopy (TEM). At 5 weeks of age, overall ultrastructural of Purkinje cells of *Sel1L*^{Pcp2Cre} mice were largely normal, including the ER, albeit being slightly dilated, compared with those of WT littermates (Figure 5A, quantitated in Figure 5D). At 9 weeks of age, dramatic changes have taken place in Purkinje cells of *Sel1L*^{Pcp2Cre} mice: dilated ER (quantified in Figure 5D), fragmented nuclei, and the presence of electrodense particles in the cytosol, possibly associated with the accumulation of protein aggregates (Figure 5, B and C). In addition, TUNEL assay showed elevated cell death in both Purkinje cells and granular layers of *Sel1L*^{Pcp2} mice at 12 weeks of age (Figure 5, E and F) but not at 5 weeks of age (data not shown). These results show that SEL1L deficiency in Purkinje cells leads to a progressive organellar dysfunction and cell death with age.

Elevated astrocyte activation and presence of microglia in Sel1L-deficient cerebellum. During the neurodegenerative process, damaged neurons release inflammatory signals that can activate glial populations,

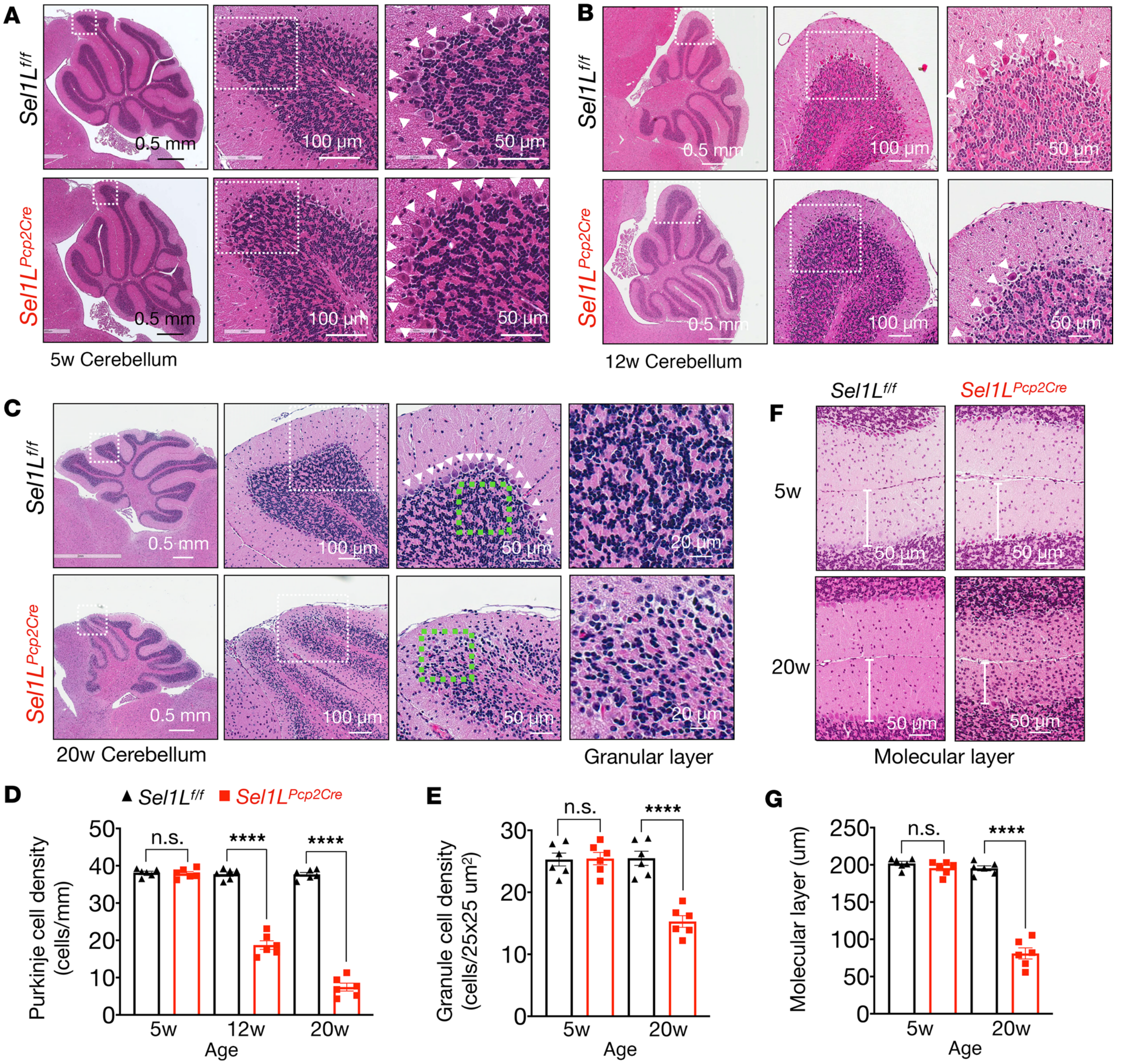

Figure 3. Purkinje cell *SEL1L* deletion leads to Purkinje cell loss and degeneration of the granular layer. (**A**–**C**) H&E-stained sagittal sections of the cerebellum from 5- (**A**), 12- (**B**), and 20-week-old mice (**C**). White arrowheads indicate Purkinje cells. (**D**) Quantitation of Purkinje cell density in H&E-stained sagittal sections of the cerebellums of mice at 5, 12, and 20 weeks of age (n = 6 mice per group). (**E**) Quantitation of granular cells in an area of 25 μm × 25 μm on the granular layer of the cerebellum (n = 6 mice per group). (**F**) Representative images of the molecular layer at 5 and 20 weeks of age, with quantitation of molecular layer thickness shown in **G** (n = 6 mice per group). Data are shown as the mean ± SEM. ****$P < 0.0001$ by 2-way ANOVA followed by Bonferroni's multiple comparisons test (**D**, **E**, and **G**). Scale bar: 0.5 mm (**A**–**C**, first column); 20 μm (**C**, fourth column); 50 μm (**A**–**C**, third column, and **F**); 100 μm (**A**–**C**, second column).

such as glial fibrillary acidic protein–positive (GFAP-positive) astrocytes (known as Bergmann glia in the cerebellum) and ionized calcium-binding adaptor molecule 1–positive (IBA1-positive) microglial cells (53, 54). Confocal microscopic analyses revealed a marked increase in GFAP signals in areas with loss of Purkinje cells in 20-week-old *Sel1L*^{Pcp2} mice (Figure 6A). This finding was further supported by Western blot analysis, which showed a 4-fold increase of GFAP protein levels in *Sel1L*^{Pcp2} mice at 12 and 20 weeks of age, but not at 5 weeks of age, compared with those in WT littermates (Figure 6, B and C). Moreover, microglial cells progressively increased in *Sel1L*^{Pcp2} mice from 5 to 12 weeks of age, accompanied by hypertrophy of cell bodies and thickening of their processes (Figure 6, D–F). Taken together, these data demonstrate that SEL1L deficiency in Purkinje cells leads to not only the loss of Purkinje cells, but also a concomitant increase of neuroinflammation within the cerebellum.

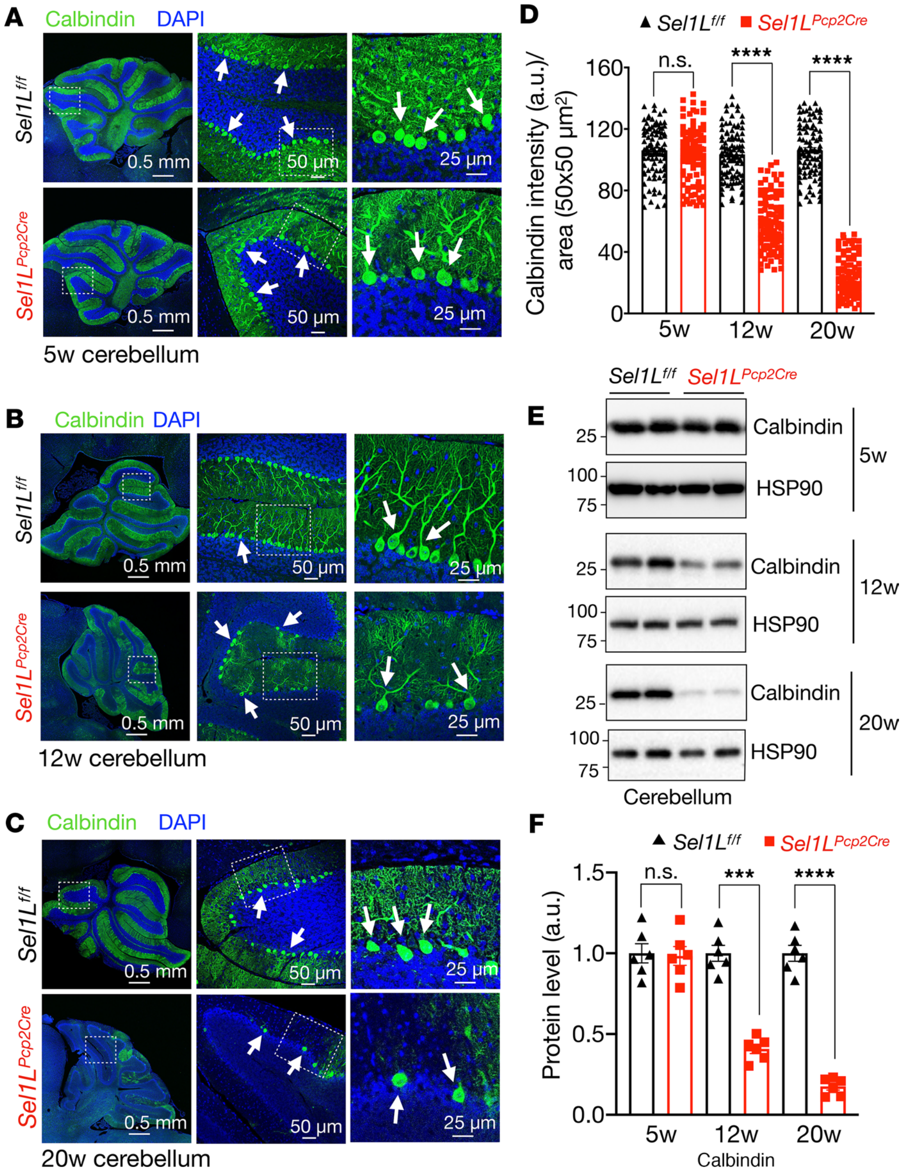

Figure 4. SEL1L deletion leads to a progressive reduction of calbindin-positive Purkinje cells in the cerebellum. (**A**–**C**) Representative confocal images of calbindin (green) and DAPI (blue) staining in the cerebellum of 5- (**A**),12- (**B**), and 20-week-old (**C**) mice. White arrows indicate calbindin-positive Purkinje cells. The magnification of the selected regions is showed in the lateral panel for each image. (**D**) Quantitation of calbindin signal intensity in the cerebellar cortex of 5-,12-, and 20-week-old mice (total of 180–200 cells from $n = 3$ mice each cohort). (**E**) Western blot analysis of calbindin and HSP90 proteins in protein extracts from cerebellum of 5-, 12- and 20-week-old mice. Values shown are in kDa. Quantitation of calbindin levels normalized to loading control is showed in **F** ($n = 6$ mice per group). Data are shown as the mean ± SEM. *$P < 0.05$, **$P < 0.01$, ***$P < 0.001$, ****$P < 0.0001$ by 2-way ANOVA followed by Bonferroni's multiple comparisons test (**D** and **F**). Scale bar: 0.5 mm (**A**–**C**, first column); 25 µm (**C**, third column); 50 µm (**A**–**C**, second column).

Altered ER homeostasis in Sel1L-deficient Purkinje cells. Finally, we examined the ER homeostasis in the *Sel1L*^{Pcp2} mice at 5 weeks of age. The unfolded protein response (UPR) and ERAD are 2 essential components of the protein quality control system (2). The accumulation of unfolded or misfolded proteins in the ER induces the activation of URP sensors such as IRE1α and PERK. While IRE1α protein level was moderately elevated (Figure 7A), there was no significant increase in IRE1α-mediated splicing of the downstream effector *Xbp1* mRNA in the cerebellum of *Sel1L*^{Pcp2} mice at 5 weeks of age (Figure 7, C and D). Similarly, while PERK protein level was significantly increased in the cerebellum of *Sel1L*^{Pcp2} mice (Figure 7, A and B), there were no significant changes in the expression of its downstream effectors, such as phosphorylation of eIF2α, ATF4, and CHOP (Figure 7, A and B).

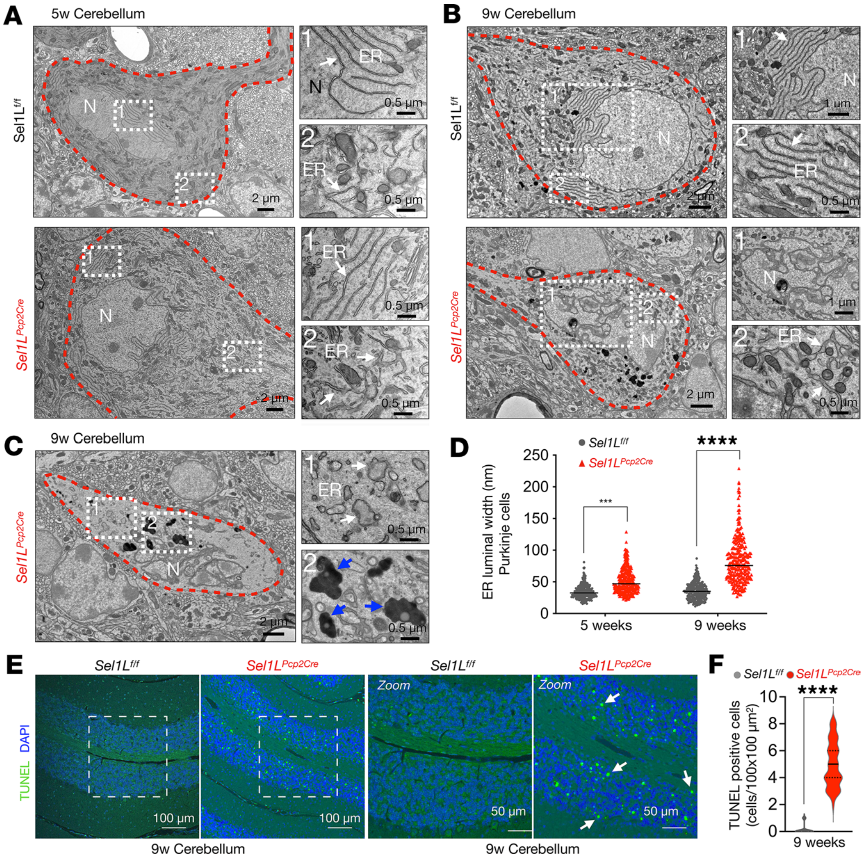

Figure 5. ER expansion and Purkinje cell neurodegeneration in *Sel1L*^{Pcp2Cre} mice. (**A**) Representative TEM images of WT and Sel1L-deficient Purkinje cells (highlighted by red dotted lines) from 5-week-old mice. High-magnification images (marked as 1 and 2) show the endoplasmic reticulum (ER; white arrows) in 2 different locations of the cell (*n* = 3 mice per group). (**B**) Representative TEM images of WT and Sel1L-deficient Purkinje cells showing fragmentation of the nucleus (N) and ER expansion at 9 weeks of age (*n* = 3 mice per group). (**C**) Representative TEM images of Sel1L-deficient Purkinje cells showing ER expansion and accumulation of electrodense structures (blue arrows) at 9 weeks of age (*n* = 3 mice per group). (**D**) Quantification of luminal ER width in TEM images of mice at 5 and 9 weeks of age (250–300 measurements from 10 cells, *n* = 3 mice per group). (**E**) Representative fluorescence images of TUNEL-labeled and DAPI-stained sagittal cerebellar sections of *Sel1L*$^{f/f}$ and *Sel1L*^{Pcp2} mice at 9 weeks of age. Higher-magnification images of selected areas are showed to the left. White arrows indicate TUNEL-positive labeled nuclei. (**F**) Quantitation of TUNEL-positive cells in the cerebellum of 9-week-old mice (*n* = 3 mice per group). Data are shown as the mean ± SEM. ***$P < 0.001$, ****$P < 0.0001$, by 2-way ANOVA followed by Bonferroni's multiple comparisons test (**D**) and *t* test (**F**). Scale bar: 0.5 µm (**A**, second column; **B**, second column, images marked as 2; and **C**, second column); 1 µm (**B**, second column, images marked as 1); 2 µm (**A**–**C**, first column); 50 µm (**E**, third and fourth image); 100 µm (**E**, first and second image).

Additionally, protein levels of the ER chaperones BiP and GRP94 were significantly elevated in the cerebellum of *Sel1L*^{Pcp2} mice at 5 weeks of age (Figure 7, E and F). This finding was further corroborated by confocal microscopic analyses showing increased KDEL (ER chaperones) and BiP protein levels in Purkinje cells of *Sel1L*^{Pcp2} mice (Figure 7, G–J). Therefore, we conclude that SEL1L deficiency resets ER homeostasis in Purkinje cells.

Discussion

Our recent studies identified several patients carrying the SEL1L or HRD1 variants with hypotonia or ataxia (36, 37), but the role of SEL1L-HRD1 ERAD in the pathogenesis of cerebellar ataxia remain unknown. Using a Purkinje cell–specific KO mouse model, here we provide definitive evidence for the essential role of SEL1L-HRD1 ERAD in Purkinje cell neurodegeneration and cerebellar ataxia in mice. *Sel1L*^{Pcp2} mice develop early-onset, progressive cerebellar ataxia, characterized by a progressive loss of Purkinje cells, neuroinflammation, and cerebellar degeneration — mirroring the characteristics of cerebellar ataxia in patients (43). This study demonstrates that SEL1L-HRD1 ERAD in Purkinje cells play an essential role in the pathogenesis of cerebellar ataxia.

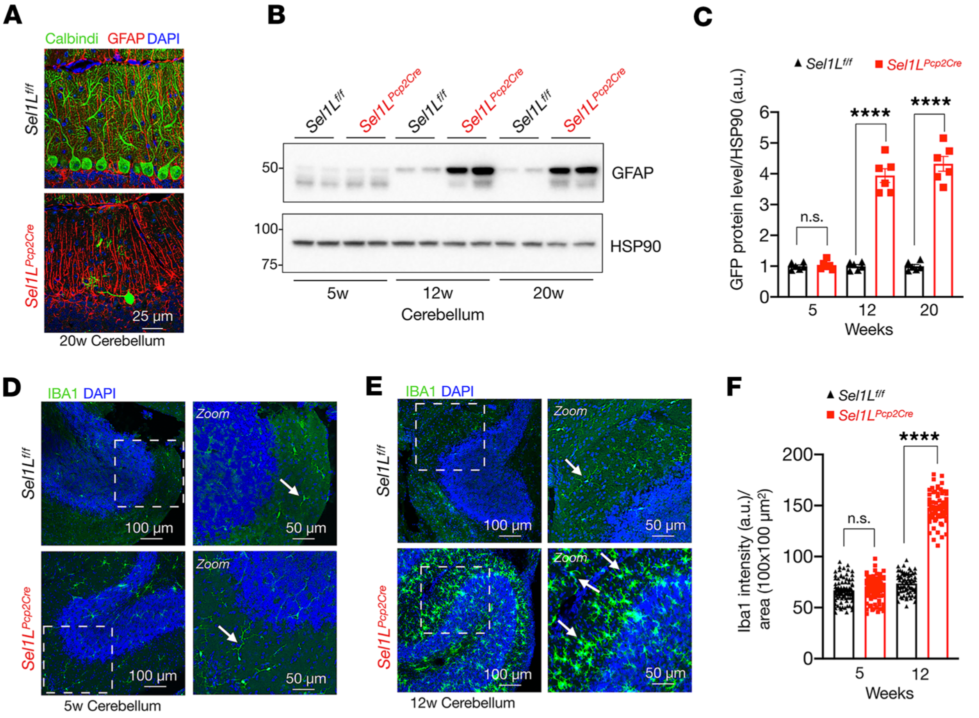

Figure 6. Elevated astrocyte activation and microglia proliferation in *Sel1L*^{Pcp2Cre} mice. (**A**) Confocal images of Purkinje cells stained with calbindin (green) and GFAP for astrocyte cells (red) in *Sel1L*$^{f/f}$ and *Sel1L*^{Pcp2} mice at 20 weeks of age (n = 3 mice per group). (**B**) Western blot analysis of GFAP in the cerebellum of 5-, 12-, and 20-week-old mice, with quantitation shown in **C** (n = 6 per group). Values shown are in kDa. (**D** and **E**) Confocal images of IBA1-positive microglia (green) and DAPI (blue) staining in the cerebellum of 5- (**D**) and 12-week-old (**E**) mice (n = 3 mice per group). Arrows indicate microglial cells. (**F**) Quantitation of IBA1-positive microglia cells in the cerebellum of 5- and 12-week-old mice. Data are shown as the mean ± SEM. *$P < 0.05$, **$P < 0.01$, ***$P < 0.001$, ****$P < 0.0001$, by 2-way ANOVA followed by Bonferroni's multiple comparisons test (**C** and **F**). Scale bar: 25 μm (**A**); 50 μm (**D** and **E**, second column); 100 μm (**D** and **E**, first column).

Purkinje cells are some of the largest neurons in the brain, with a prominent ER structure that forms an interconnected network regulating calcium signaling, protein synthesis, folding, and protein trafficking (55). Previous studies have shown that Purkinje cells are particularly vulnerable to alterations in ER homeostasis due to their high demand for protein synthesis needed to maintain a large number of synapsis (56, 57). Our data indicate that Purkinje cells cannot adapt to a significant reduction in SEL1L-HRD1 ERAD function, ultimately leading to cell death. One potential detrimental effect of SEL1L-HRD1 ERAD loss in Purkinje cells could be the accumulation of misfolded proteins in the ER, resulting in cell death due to chronic ER stress. In this context, we observed an accumulation of ER chaperones, such as BiP and Grp94, and evidence of dilated ER by TEM. However, we did not detect an active UPR, as indicated by the absence of Xbp-1 mRNA splicing, a downstream effector of IRE1α, or changes in ATF4, CHOP, or eIF2α, 3 common downstream effectors of the PERK pathway. These results may suggest that additional mechanism independent of ER stress may contribute to the degeneration and cell death of Purkinje cells. In previous studies, we reported pathological changes associated with the accumulation and ER retention of ERAD substrates (12, 15, 20, 23, 26, 32, 33, 58, 59) and mitochondria dysfunction in ERAD-deficient cells (30). We hypothesize that alterations in the biosynthesis of specific factors involved in maintaining active synapsis, cell-cell interactions, or the reduction of active neurotrophic receptors could also contribute to Purkinje cell death (60, 61). We are currently exploring different approaches to isolate and identify ERAD-specific substrates in Purkinje cells. Future studies using single-cell analysis could help identify specific alterations of Purkinje cells, granular cells, and glial cells during the progression of cerebellar ataxia in *Sel1L*^{Pcp2} mice.

We also observed compelling evidence of robust astrocyte activation and an elevated number of microglia associated with the loss of Purkinje cells in the cerebellum of Sel1L^{Pcp2Cre} mice. Bergmann glia, an unusual type of astrocyte, are closely associated with Purkinje cells, enclosing both soma and synapses

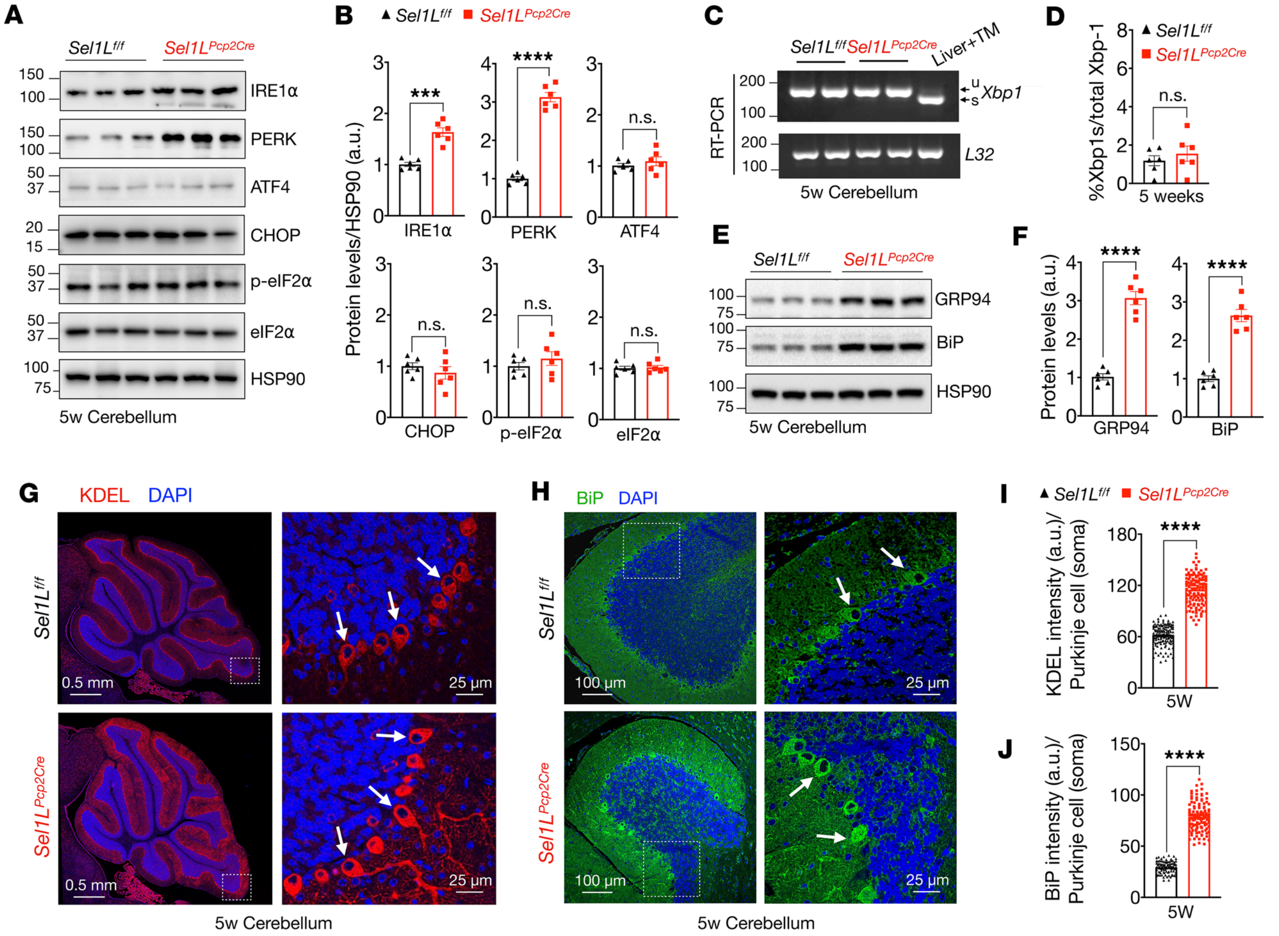

Figure 7. Sel1L deficiency is associated with mild UPR in Purkinje cells of *Sel1L*^{Pcp2Cre} mice. (**A**) Western blot analysis of the UPR sensors IRE1α and PERK, including ATF4, CHOP, and eIF2α pathways in the cerebellums of mice at 5 weeks of age, with quantitation shown in **B** (*n* = 6 mice per group). Values shown are in kDa. (**C**) RT-PCR of *Xbp1* mRNA splicing in the cerebellum of 5-week-old mice. u and s indicate the unspliced and spliced form of *Xbp1*. Liver treated with tunicamycin (TM, ER stress inducer) was used as a positive control. Quantitation of the spliced form of Xbp1 (Xbp1s) is shown in **D** (*n* = 6 mice per group). (**E**) Western blot analysis of the ER chaperones GRP94 and BiP in cerebellum from 5-week-old mice, with quantitation shown in **F** (*n* = 6 mice per group). (**G** and **H**) Representative confocal images of KDEL (red signal) and BiP (green signal, shown in **H**) in the cerebellum of 5-week-old mice. White arrows indicate Purkinje cells (*n* = 3 per group). (**I** and **J**) Quantitation of KDEL (**I**) and BiP (**J**) signal intensity in the soma of Purkinje cells (total of 120–150 cells from *n* = 3 mice each cohort). Data are shown as the mean ± SEM. ***$P < 0.001$, ****$P < 0.0001$, by *t* test. Scale bar: 0.5 μm (**G**, first column); 25 μm (**G** and **H**, second column); 100 μm (**H**, first column).

and establishing complex anatomical and functional interactions (62). The typical radial appearance of Bergmann glia and normal dendritic tree pattern of Purkinje cells was observed in 5-week-old animals, suggesting a normal postnatal development of the cerebellum. Normal levels of GFAP and IBA1 markers were detected in 5-week-old mice, suggesting absence of neuroinflammation at this age. However, at 12 weeks of age, we found elevated levels of GFAP and an increased number of microglia in Sel1L^{Pcp2Cre} mice, which correlated with a reduction in the number of Purkinje cells and the development of ataxia. We suspect that dysfunctional Purkinje cells could release inflammatory signals that trigger the activation of Bergmann glia. Activated astrocytes may lead to alterations in neurotransmitter balance and neurotrophic support, ultimately affecting the function and survival of Purkinje cells (54). Similarly, activated microglia can release pro-inflammatory cytokines, which can induce neuronal cell death pathways, including apoptosis and necrosis, when chronically elevated (63). Microglia has the ability to engulf and digest cellular debris, including dying neurons and their synapsis. Excessive removal of synapsis could also lead to synaptic dysfunction and ultimately contributing to Purkinje cells loss (63). This observation aligns with other neurodegenerative diseases characterized by neuroinflammation, such as multiple sclerosis, Alzheimer's disease, and amyotrophic lateral sclerosis, where astrocytes and microglia are key regulators of the inflammatory response and diseases progression (54). We envision a possible scenario where partially impaired

Purkinje cells may trigger Bergmann glia and microglia activation, which in turn could exacerbate Purkinje cell dysfunction, resulting in a vicious feed-forward cycle of Purkinje and granule cell neurodegeneration. Future studies will investigate how Sel1L deficiency in Purkinje cells leads to the activation of astrocytes and microglia in vivo.

Our findings indicate a key role of SEL1L-HRD1 ERAD in Purkinje cells in the development of cerebellar ataxia. This observation is consistent with a previous report in Finnish Hounds with cerebellar ataxia carrying a biallelic *SEL1L*^{S658P} variant (39), which indeed leads to early-onset, nonprogressive cerebellar ataxia in mice, as we recently demonstrated (40). Additionally, we have identified several patients with SEL1L M528R variant displaying ataxia, while others with SEL1L G585D or HRD1 P398L show mild hypotonia (36). The varying clinical presentations among these patients likely stem from differing degrees of ERAD dysfunction caused by these variants (37). Collectively, these studies underscore the potential pathogenic impact of SEL1L-HRD1 ERAD dysfunction. While none of these disease variants is linked to obvious UPR activation (36, 37), future studies are needed to delineate the underlying mechanisms, which may involve substrate- and cell-type-specific effect contributing to this pathological process.

Methods

Sex as a biological variable. Our study examined male and female animals, and similar findings are reported for both sexes.

Mice. Purkinje cell–specific *Sel1L*-deficient (*Sel1L*^{Pcp2Cre}) mice were generated by crossing *Pcp2*-Cre mice on the C57BL/6J background (The Jackson Laboratories, 004146) with *Sel1L*$^{fl/fl}$ mice on the C57BL/6J background (*7*). *Pcp2*-Cre mice were donated by Andrew P. Lieberman at the University of Michigan. Age- and sex-matched littermates were maintained in a temperature-controlled room on a 12-hour-light/dark cycle and used in all studies.

Genotyping. Mice were routinely genotyped using PCR of genomic DNA samples obtained from ears with the following primer pairs: *Sel1L*$^{fl/fl}$: F: 5′-CTGACTGAGGAAGGGTCTC-3′, R: 5′-GCTAAAAACATTACAAAGGGGCA-3′; Cre recombinase: F: 5′-ACCTGAAGATGTTCGCGATTATCT-3′, R: 5′-ACCGTCAGTACGTGAGATATCTT-3′.

Behavioral studies. Most behavior procedures were performed by investigators blinded to the genotypes as previously described (40). For hindlimb clasping assessment, mice were lifted by tails and held over a cage for 1 minute to assess abnormal hind limb clasping and scored as previously described (49). The footprints were analyzed for stride length (the distance covered by the same hind paw), stride width (the distance from one hind limb that intersects perpendicularly with the line for stride length on the contralateral hind paw), paw-matched distance (the distance between hind and forepaw), and the ratio between stride length and width. All mice received 3 trainings and a trial run. The balance beam study was used to evaluate motor coordination and balance as previously described (40). Mice were trained to stay upright and walk across an elevated narrow beam to a safe platform for 2 consecutive days (3 times per day). On the third day, the time to cross 80 cm on the beam was measured. A video camera was set on a tripod to record the performance of the animals during the test. Room temperature, humidity, lighting, and background noise were kept consistent throughout the experiment.

Western blot and antibodies. Tissues were harvested and snap-frozen in liquid nitrogen. The proteins were extracted by sonication in NP-40 lysis buffer (50 mM Tris-HCL at pH 7.5, 150 mM NaCl, 1% NP-40, 1 mM EDTA) with protease inhibitor (MilliporeSigma), DTT (MilliporeSigma, 1 mM), and phosphatase inhibitor cocktail (MilliporeSigma). Lysates were incubated on ice for 30 minutes and centrifuged at 16,000*g* for 10 minutes. Supernatants were collected and analyzed for protein concentration using the Bio-Rad Protein Assay Dye. 20–50 μg protein was denatured at 95°C for 5 minutes in 5x SDS sample buffer (250 mM Tris-HCl pH 6.8, 10% sodium dodecyl sulfate, 0.05% bromophenol blue, 50% glycerol, and 1.44 M b-mercaptoethanol). Protein was separated on SDS-PAGE, followed by electrophoretic transfer to PVDF (Fisher Scientific) membrane. The blots were incubated in 2% BSA/Tris-buffered saline Tween-20 (TBST) with primary antibodies overnight at 4°C: anti-HSP90 (Santa Cruz, sc-7947, 1:5,000), anti-SEL1L (homemade, 1:10,000) (33), anti-HRD1 (Proteintech, 13473-1, 1:2,000), anti-OS9 (Abcam, ab109510, 1:5,000), anti-IRE1α (Cell Signaling, 3294, 1:2,000), anti-PERK (Cell Signaling, 3192, 1:1,000), anti-Calbindin (Cell Signaling, 2173, 1:5,000), anti-GFAP (Cell Signaling, 3670, 1:2,000), anti-ATF4 (Cell Signaling, 11815, 1:1,000), anti-CHOP (Cell Signaling, 2895, 1:1,000), anti-eIF2α (Cell Signaling, 9722, 1:1,000), and anti-p-eIF2α (Cell Signaling, 9721, 1:1,000). GRP94 and BiP proteins were detected using anti-KDEL antibody (Novus Biologicals, 97469, 1:1,000). Membranes were washed with TBST and incubated with HRP-conjugated secondary antibodies

(Bio-Rad, 1:10,000) at room temperature for 1 hour for ECL chemiluminescence detection system (Bio-Rad) development. Band intensity was determined using Image lab (Bio-Rad) software.

RNA preparation and RT-PCR. Total RNA was extracted from tissues and cells using TRI Reagent and BCP phase separation reagent per supplier's protocol (Molecular Research Center, TR 118). RT-PCR for *Xbp1* mRNA splicing was performed as previously described (15). The ratio of Xbp1s level to total Xbp1 (Xbp1u + Xbp1s) level was quantified by Image Lab (Bio-Rad) software. RT-PCR primer sequences are as follows: mXbp1 F: ACGAGGTTCCAGAGGTGGAG, R: AAGAGGCAACAGTGTCAGAG; mL32 F: GAGCAACAAGAAAACCAAGCA, R: TGCACACAAGCCATCTACTCA.

Histology. Anesthetized mice were perfused with 20 mL of 0.9% NaCl followed by 40 mL of 4% paraformaldehyde in 0.1 M PBS pH 7.4 for fixation. Brains were dissected and fixed overnight in 4% paraformaldehyde in PBS at 4°C. For H&E staining, samples were dehydrated, embedded in paraffin, and stained at the Rogel Cancer Center Tissue and Molecular Pathology Core or In-Vivo Animal Core at the University of Michigan Medical School. Quantification of Purkinje cell loss was performed on H&E-stained sections. Counts were normalized to the length of the Purkinje layer, as measured by Aperio ImageScope software, and shown as Purkinje cell density.

Immunofluorescence staining. Paraffin-embedded brain sections were deparaffinized in xylene and rehydrated using a graded ethanol (100%, 90%, 70%), followed by a rinse in distilled water. Slides were boiled for antigen retrieval in sodium citrate buffer in a microwave. Sections were then incubated in a blocking solution (5% donkey serum, 0.3% Triton X-100 in PBS) for 1 hour at room temperature and with the following primary antibodies in a humidifying chamber overnight at 4°C: anti-Calbindin (Cell Signaling, 2173, 1:100), anti-KDEL (Novus Biologicals, 97469, 1:200), anti-SEL1L (homemade, 1:100), anti-BiP (Abcam, 21685, 1:100), anti-GFAP (Cell Signaling, 3670, 1:100), and IBA1 (Novus Biologicals, NB100-1028, 1:100). The next day, following 3 washes with PBST (0.03% Triton X-100 in PBS), slides were incubated with the respective Alexa Fluor conjugated to secondary antibodies (Jackson ImmunoResearch, 1:500) for 1 hour at room temperature, followed by mounting with VECTASHIELD mounting medium containing DAPI (Vector Laboratories, H-1500). Images were captured using a Nikon A1 confocal microscope at the University of Michigan Morphology and Image Analysis Core. Relative protein levels in immunofluorescence images were quantified using FIJI-ImageJ software (64).

TEM. Mice were anesthetized and perfused with 3% glutaraldehyde, 3% formaldehyde in 0.1 M cacodylate buffer (Electron Microscopy Sciences, 16220, 15710, 11653). Cerebellum was dissected, cut into small pieces, and fixed overnight at 4°C in 3% glutaraldehyde, 3% formaldehyde in 0.1 M Sorenson's buffer (Electron Microscopy Sciences, 11682). The tissues were then prepared, embedded, and sectioned at the University of Michigan Histology and Imaging Core. Samples were stained with uranyl acetate/lead citrate, and high-resolution images were acquired with a JEOL 1400-plus electron microscope.

Statistics. Statistics tests were performed in GraphPad Prism (version 8.0). Unless indicated otherwise, values are presented as mean ± SEM. All experiments have been repeated at least 3 times and/or performed with multiple independent biological samples from which representative data are shown. All datasets passed normality and equal variance tests. Statistical differences between the groups were compared using the unpaired 2-tailed Student's t test for 2 groups or 2-way ANOVA with Bonferroni's multiple comparison test for multiple groups. $P < 0.05$ was considered statistically significant.

Study approval. All animal procedures were approved by the Institutional Animal Care and Use Committee of the University of Michigan Medical School (PRO00010658) and the University of Virginia (4459).

Data available. All data and materials for this manuscript are included in the Methods and Supporting Data Values. Materials and reagents are freely available upon request.

Author contributions

MT, HW, and BP collaboratively designed and performed most experiments. LLL, HHW, and ABL assisted with some in vitro and in vivo experiments. ZZ provided insightful discussion. LQ directed the study and wrote the manuscript with help from MT, HW, and BP. BP, HW, ABL, and MT wrote the Methods and figure legends. All authors commented on and approved the manuscript.

Acknowledgments

We acknowledge members of LQ's and Peter Arvan's laboratories at the University of Michigan Medical School for technical assistance and insightful discussions and the University of Michigan Animal

Phenotyping Core for some of the behavioral tests (supported by National Institute of Diabetes and Digestive and Kidney Diseases P30 grants DK020572, DK089503, and 1U2CDK135066). This work was supported by National Institute of Neurological Disorders and Stroke RF1NS122060 (to ZZ), National Institute of Aging 1R01AG089640 (to LQ and ZZ), and National Institute of General Medical Sciences 1R35GM130292 and Alzheimer's Association 24AARG-D-NTF-1187603 (to LQ). LLL was supported in part by National Ataxia Foundation (NAF 918037).

Address correspondence to: Ling Qi, 480 Ray C. Hunt Drive, Charlottesville, Virginia 22903, USA. Email: xvr2hm@virginia.edu.

---

1. Olzmann JA, et al. The mammalian endoplasmic reticulum-associated degradation system. *Cold Spring Harb Perspect Biol*. 2013;5(9):a013185.
2. Hwang J, Qi L. Quality control in the endoplasmic reticulum: crosstalk between ERAD and UPR pathways. *Trends Biochem Sci*. 2018;43(8):593–605.
3. Qi L, et al. New insights into the physiological role of endoplasmic reticulum-associated degradation. *Trends Cell Biol*. 2017;27(6):430–440.
4. Hampton RY, et al. Role of 26S proteasome and HRD genes in the degradation of 3-hydroxy-3-methylglutaryl-CoA reductase, an integral endoplasmic reticulum membrane protein. *Mol Biol Cell*. 1996;7(12):2029–2044.
5. Bordallo J, et al. Der3p/Hrd1p is required for endoplasmic reticulum-associated degradation of misfolded lumenal and integral membrane proteins. *Mol Biol Cell*. 1998;9(1):209–222.
6. Kikkert M, et al. Human HRD1 is an E3 ubiquitin ligase involved in degradation of proteins from the endoplasmic reticulum. *J Biol Chem*. 2004;279(5):3525–3534.
7. Sun S, et al. Sel1L is indispensable for mammalian endoplasmic reticulum-associated degradation, endoplasmic reticulum homeostasis, and survival. *Proc Natl Acad Sci U S A*. 2014;111(5):E582–E591.
8. Gardner RG, et al. Endoplasmic reticulum degradation requires lumen to cytosol signaling. Transmembrane control of Hrd1p by Hrd3p. *J Cell Biol*. 2000;151(1):69–82.
9. Francisco AB, et al. Deficiency of suppressor enhancer Lin12 1 like (SEL1L) in mice leads to systemic endoplasmic reticulum stress and embryonic lethality. *J Biol Chem*. 2010;285(18):13694–13703.
10. Yagishita N, et al. Essential role of synoviolin in embryogenesis. *J Biol Chem*. 2005;280(9):7909–7916.
11. Fujita H, et al. The E3 ligase synoviolin controls body weight and mitochondrial biogenesis through negative regulation of PGC-1β. *EMBO J*. 2015;34(8):1042–1055.
12. Sha H, et al. The ER-associated degradation adaptor protein Sel1L regulates LPL secretion and lipid metabolism. *Cell Metab*. 2014;20(3):458–470.
13. Wu T, et al. Hrd1 suppresses Nrf2-mediated cellular protection during liver cirrhosis. *Genes Dev*. 2014;28(7):708–722.
14. Yang H, et al. Hrd1-mediated BLIMP-1 ubiquitination promotes dendritic cell MHCII expression for CD4 T cell priming during inflammation. *J Exp Med*. 2014;211(12):2467–2479.
15. Sun S, et al. IRE1α is an endogenous substrate of endoplasmic-reticulum-associated degradation. *Nat Cell Biol*. 2015;17(12):1546–1555.
16. Ji Y, et al. The Sel1L-Hrd1 endoplasmic reticulum-associated degradation complex manages a key checkpoint in B cell development. *Cell Rep*. 2016;16(10):2630–2640.
17. Sun S, et al. Epithelial Sel1L is required for the maintenance of intestinal homeostasis. *Mol Biol Cell*. 2016;27(3):483–490.
18. Kong S, et al. Endoplasmic reticulum-resident E3 ubiquitin ligase Hrd1 controls B-cell immunity through degradation of the death receptor CD95/Fas. *Proc Natl Acad Sci U S A*. 2016;113(37):10394–10399.
19. Xu Y, et al. The ER membrane-anchored ubiquitin ligase Hrd1 is a positive regulator of T-cell immunity. *Nat Commun*. 2016;7:12073.
20. Shi G, et al. ER-associated degradation is required for vasopressin prohormone processing and systemic water homeostasis. *J Clin Invest*. 2017;127(10):3897–3912.
21. Bhattacharya A, et al. Hepatic Sel1L-Hrd1 ER-associated degradation (ERAD) manages FGF21 levels and systemic metabolism via CREBH. *EMBO J*. 2018;37(22):e99277.
22. Wei J, et al. HRD1-ERAD controls production of the hepatokine FGF21 through CREBH polyubiquitination. *EMBO J*. 2018;37(22):e98942.
23. Kim GH, et al. Hypothalamic ER-associated degradation regulates POMC maturation, feeding, and age-associated obesity. *J Clin Invest*. 2018;128(3):1125–1140.
24. Bhattacharya A, Qi L. ER-associated degradation in health and disease - from substrate to organism. *J Cell Sci*. 2019;132(23):jcs232850.
25. Liu L, et al. ER-associated degradation preserves hematopoietic stem cell quiescence and self-renewal by restricting mTOR activity. *Blood*. 2020;136(26):2975–2986.
26. Shrestha N, et al. Sel1L-Hrd1 ER-associated degradation maintains β cell identity via TGF-β signaling. *J Clin Invest*. 2020;130(7):3499–3510.
27. Shrestha N, et al. Endoplasmic reticulum protein quality control in β cells. *Semin Cell Dev Biol*. 2020;103:59–67.
28. Xu L, et al. Protein quality control through endoplasmic reticulum-associated degradation maintains haematopoietic stem cell identity and niche interactions. *Nat Cell Biol*. 2020;22(10):1162–1169.
29. Wu T, et al. HRD1, an important player in pancreatic β-cell failure and therapeutic target for type 2 diabetic mice. *Diabetes*. 2020;69(5):940–953.

30. Zhou Z, et al. Endoplasmic reticulum-associated degradation regulates mitochondrial dynamics in brown adipocytes. *Science*. 2020;368(6486):54–60.
31. Liu X, et al. Notch-induced endoplasmic reticulum-associated degradation governs mouse thymocyte β-selection. *Elife*. 2021;10:e69975.
32. Yoshida S, et al. Endoplasmic reticulum-associated degradation is required for nephrin maturation and kidney glomerular filtration function. *J Clin Invest*. 2021;131(7):e143988.
33. Abdon B, et al. Muscle-specific ER-associated degradation maintains postnatal muscle hypertrophy and systemic energy metabolism. *JCI Insight*. 2023;8(17):e170387.
34. Shrestha N, et al. Integration of ER protein quality control mechanisms defines β cell function and ER architecture. *J Clin Invest*. 2023;133(1):e163584.
35. Wu SA, et al. The mechanisms to dispose of misfolded proteins in the endoplasmic reticulum of adipocytes. *Nat Commun*. 2023;14(1):3132.
36. Wang HH, et al. Hypomorphic variants of SEL1L-HRD1 ER-associated degradation are associated with neurodevelopmental disorders. *J Clin Invest*. 2024;134(2):e170054.
37. Weis D, et al. Biallelic Cys141Tyr variant of SEL1L is associated with neurodevelopmental disorders, agammaglobulinemia, and premature death. *J Clin Invest*. 2024;134(2):e170882.
38. Umphred-Wilson K, Adoro S. Hypomorphic human SEL1L and HRD1 variants uncouple multilayered ER-associated degradation machinery. *J Clin Invest*. 2024;134(2):e175448.
39. Kyostila K, et al. A SEL1L mutation links a canine progressive early-onset cerebellar ataxia to the endoplasmic reticulum-associated protein degradation (ERAD) machinery. *PLoS Genet*. 2012;8(6):e1002759.
40. Lin LL, et al. SEL1L-HRD1 interaction is required to form a functional HRD1 ERAD complex. *Nat Commun*. 2024;15(1):1440.
41. Jayadev S, Bird TD. Hereditary ataxias: overview. *Genet Med*. 2013;15(9):673–683.
42. Beckinghausen J, Sillitoe RV. Insights into cerebellar development and connectivity. *Neurosci Lett*. 2019;688:2–13.
43. Koeppen AH. The neuropathology of the adult cerebellum. *Handb Clin Neurol*. 2018;154:129–149.
44. Gandhi J, et al. Protein misfolding and aggregation in neurodegenerative diseases: a review of pathogeneses, novel detection strategies, and potential therapeutics. *Rev Neurosci*. 2019;30(4):339–358.
45. Zambonin JL, et al. Spinocerebellar ataxia type 29 due to mutations in ITPR1: a case series and review of this emerging congenital ataxia. *Orphanet J Rare Dis*. 2017;12(1):121.
46. Ando H, et al. Aberrant IP_3 receptor activities revealed by comprehensive analysis of pathological mutations causing spinocerebellar ataxia 29. *Proc Natl Acad Sci U S A*. 2018;115(48):12259–12264.
47. Barski JJ, et al. Cre recombinase expression in cerebellar Purkinje cells. *Genesis*. 2000;28(3–4):93–98.
48. Slugocka A, et al. Genetic targeting in cerebellar purkinje cells: an update. *Cerebellum*. 2017;16(1):191–202.
49. Guyenet SJ, et al. A simple composite phenotype scoring system for evaluating mouse models of cerebellar ataxia. *J Vis Exp*. 2010;(39):1787.
50. Wetts R, Herrup K. Interaction of granule, Purkinje and inferior olivary neurons in lurcher chimaeric mice. I. Qualitative studies. *J Embryol Exp Morphol*. 1982;68:87–98.
51. Hamre KM, West JR. The effects of the timing of ethanol exposure during the brain growth spurt on the number of cerebellar Purkinje and granule cell nuclear profiles. *Alcohol Clin Exp Res*. 1993;17(3):610–622.
52. Lalonde R, Strazielle C. Motor performances of spontaneous and genetically modified mutants with cerebellar atrophy. *Cerebellum*. 2019;18(3):615–634.
53. Sofroniew MV, Vinters HV. Astrocytes: biology and pathology. *Acta Neuropathol*. 2010;119(1):7–35.
54. Kwon HS, Koh SH. Neuroinflammation in neurodegenerative disorders: the roles of microglia and astrocytes. *Transl Neurodegener*. 2020;9(1):42.
55. Villa A, et al. The endoplasmic reticulum of Purkinje neuron body and dendrites: molecular identity and specializations for Ca2+ transport. *Neuroscience*. 1992;49(2):467–477.
56. Zhao L, et al. Alteration of the unfolded protein response modifies neurodegeneration in a mouse model of Marinesco-Sjögren syndrome. *Hum Mol Genet*. 2010;19(1):25–35.
57. Yang Y, et al. Disruption of Tmem30a results in cerebellar ataxia and degeneration of Purkinje cells. *Cell Death Dis*. 2018;9(9):899.
58. Ji Y, et al. SEL1L-HRD1 endoplasmic reticulum-associated degradation controls STING-mediated innate immunity by limiting the size of the activable STING pool. *Nat Cell Biol*. 2023;25(5):726–739.
59. Bhattacharya A, et al. SEL1L-HRD1 ER-associated degradation suppresses hepatocyte hyperproliferation and liver cancer. *iScience*. 2022;25(10):105183.
60. Baptista CA, et al. Cell-cell interactions influence survival and differentiation of purified Purkinje cells in vitro. *Neuron*. 1994;12(2):243–260.
61. Mount HT, et al. Glial cell line-derived neurotrophic factor promotes the survival and morphologic differentiation of Purkinje cells. *Proc Natl Acad Sci U S A*. 1995;92(20):9092–9096.
62. Bellamy TC. Interactions between Purkinje neurones and Bergmann glia. *Cerebellum*. 2006;5(2):116–126.
63. Bessis A, et al. Microglial control of neuronal death and synaptic properties. *Glia*. 2007;55(3):233–238.
64. Shihan MH, et al. A simple method for quantitating confocal fluorescent images. *Biochem Biophys Rep*. 2021;25:100916.